Geophysical Research Letters

RESEARCH LETTER
10.1029/2018GL078543

Key Points:
- Microstructure measurements from an AUV reveal transient turbulent mixing in the far-field of a plume during upwelling
- Spatial and temporal variability of dissipation and mixing is related to changing wind and tide conditions
- Alongshore shear was as important, at times, as cross-shore shear for driving mixing within the plume as it separated from the coast

Supporting Information:
- Supporting Information S1
- Data Set S1
- Data Set S2
- Data Set S3
- Data Set S4
- Data Set S5
- Data Set S6
- Data Set S7
- Data Set S8

Correspondence to:
A. W. Fisher and N. J. Nidzieko,
nidzieko@ucsb.edu;
awfisher@ucsb.edu

Citation:
Fisher, A. W., Nidzieko, N. J., Scully, M. E., Chant, R. J., Hunter, E. J., & Mazzini, P. L. F. (2018). Turbulent mixing in a far-field plume during the transition to upwelling conditions: Microstructure observations from an AUV. *Geophysical Research Letters*, *45*, 9765–9773. https://doi.org/10.1029/2018GL078543

Received 16 APR 2018
Accepted 27 AUG 2018
Accepted article online 4 SEP 2018
Published online 23 SEP 2018

Turbulent Mixing in a Far-Field Plume During the Transition to Upwelling Conditions: Microstructure Observations From an AUV

Alexander W. Fisher[1], Nicholas J. Nidzieko[1], Malcolm E. Scully[2], Robert J. Chant[3], Elias J. Hunter[3], and Piero L. F. Mazzini[4]

[1]Department of Geography, University of California, Santa Barbara, CA, USA, [2]Applied Ocean Physics and Engineering, Woods Hole Oceanographic Institution, [3]Department of Marine and Coastal Sciences, Rutgers University, New Brunswick, NJ, USA, [4]Estuary and Ocean Science Center, San Francisco State University, Tiburon, CA, USA

Abstract A REMUS 600 autonomous underwater vehicle was used to measure turbulent mixing within the far-field Chesapeake Bay plume during the transition to upwelling. Prior to the onset of upwelling, the plume was mixed by a combination of energetic downwelling winds and bottom-generated shear resulting in a two-layer plume structure. Estimates of turbulent dissipation and buoyancy flux from a nose-mounted microstructure system indicate that scalar exchange within the plume was patchy and transient, with direct wind mixing constrained to the near surface by stratification within the plume. Changing wind and tide conditions contributed to temporal variability. Following the separation of the upper plume from the coast, alongshore shear became a significant driver of mixing on the shoreward edge of the plume.

Plain Language Summary Turbulence measurements made by an autonomous underwater vehicle reveal that the wind-driven offshore movement of a coastal river plume leads to intermittent and patchy mixing of plume and shelf waters. These novel, high-resolution observations highlight the importance of capturing transient features when determining the fate of rivers on continental shelves.

1. Introduction

River plumes play a critical role in the fate of terrigenous material delivered to the coastal ocean (Horner-Devine et al., 2015). River plume dynamics depend on the entrainment of ambient seawater through vertical mixing, and so detailed observations of the rates and mechanisms of mixing are essential to understanding the impact of river-borne materials on coastal ecosystems and shelf seas.

Briefly, the three dynamical regions of a river plume are (1) the near-field, where outflow momentum exceeds plume buoyancy; (2) the mid-field, where Earth's rotation arrests the spreading of the plume and turns it downcoast; and (3) the far-field, where the plume is still distinct from ambient ocean water but is no longer controlled by outflow momentum (Horner-Devine et al., 2015). Numerous studies have examined mixing and transport within the near-field (Chen & MacDonald, 2006; Hetland, 2010; Kilcher & Nash, 2010; Kilcher et al., 2012; MacDonald et al., 2007; Nash et al., 2009) and mid-field of buoyant plumes (Chant et al., 2008; Garvine, 1987; Horner-Devine, 2009; McCabe et al., 2009; Yankovsky & Chapman, 1997), but observations of the far-field are relatively scarce (Castelao et al., 2008; Fong et al., 1997; Houghton et al., 2004; Lentz & Largier, 2006; Mazzini et al., 2014; Mazzini & Chant, 2016). The far-field is large and represents a significant area over which mixing can occur; however, the relatively low turbulence levels found there are difficult to measure, limiting understanding of total plume mixing.

The transition to upwelling conditions is a critical period for the fate of a far-field river plume because salt exchange typically peaks within one inertial period of the onset of upwelling, due to the combined influence of transient wind forcing and inertial shears (Fong & Geyer, 2001). Using direct measurements of turbulent mixing and plume structure collected by an autonomous underwater vehicle (AUV), we present some of the most detailed observations to-date of an upwelling plume, characterizing scalar exchange within the Chesapeake Bay plume during the transition from a buoyant coastal current to a surface-trapped plume at the onset of upwelling.

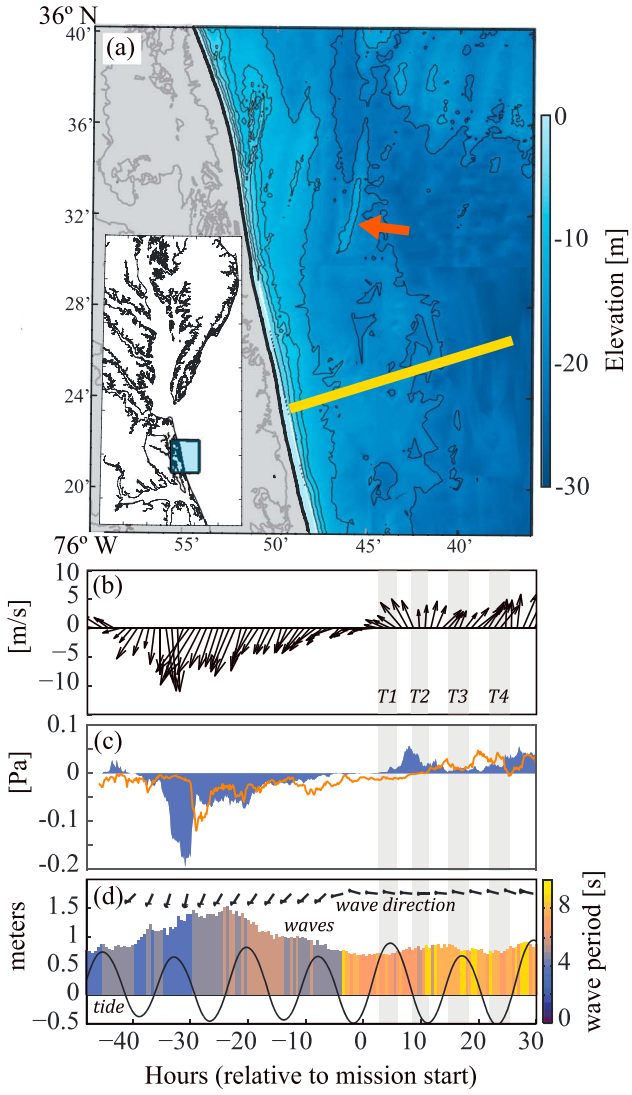

Figure 1. (a) Map of study location. Yellow bar indicates cross-shore transect, and inset shows location relative to the Chesapeake Bay. Red arrow highlights ~6 m outcrop. (b) Wind conditions indicating the direction in which the wind is blowing. Cross-shore transects shown as boxes labeled *T1–T4*. (c) Alongshore (shaded) and cross-shore components (line) of wind stress. (d) Surface waves and tides.

2. Data Collection

2.1. Experiment Overview

Data were collected using a Hydroid-Kongsberg REMUS 600 AUV, *Callinectes*. The 4-m-long propeller-driven AUV, which was launched and recovered from the *R/V Arabella* near Currituck Beach, Virginia, conducted a 32-hr mission 15–17 May 2015, completing four transits (denoted T1–T4) of a ~10-nm cross-shore transect; the shoreward terminus of this line was 36.3915°N, 75.8175°W (Figure 1a). Brackish water released from the Bay on ebb tide flows southward as a geostrophic coastal current during downwelling conditions; the transect location was far enough away from the Bay (~35 nm downcoast) that the buoyant plume was no longer controlled by the initial ebb-tide momentum from the mouth (Lentz & Largier, 2006; Valle-Levinson et al., 2001).

During the deployment, local wind and wave conditions were obtained from a meteorological station and waverider buoy at the 27-m isobath maintained by the Coastal and Hydraulics Laboratory Field Research Facility located near Duck, North Carolina. Water level measurements were obtained from NOAA tide gauge 8651371, also located at Coastal and Hydraulics Laboratory Field Research Facility.

2.2. AUV Instrumentation and Mission Sampling

In order to optimize data collection of the plume structure, the vehicle adaptively ended the outbound transit (run at a constant depth of 2 m) when the salinity reached 31.5; as a safety precaution, the maximum offshore distance was capped at 10 nm. The first three transects were determined via salinity threshold; the last transect reached the 10-nm limit. Traveling at 1.5 m/s, the vehicle executed a sawtooth pattern between 3 m above the seabed and 1.5 m below the surface on shore-bound legs. The inbound transects were spaced 6 to 8 hr apart, the first of which started ~2.8 hr after the onset of upwelling winds (Figures 1b and 1c) and corresponded roughly to high and low water within the tidal cycle (Figure 1d). Because the vehicle was ballasted to be slightly buoyant, the average pitch of the vehicle was −7.64 ± 1.78° during dives and −0.05 ± 1.96° during climbs. The vehicle's angle of attack, calculated as the difference between the vehicle's pitch and vertical trajectory (Fer et al., 2014), was −3.86 ± 2.78° and −3.89 ± 2.39° relative to vehicle trajectory during dives and climbs, respectively.

The vehicle carried a standard instrument payload that included upward- and downward-looking 600-kHz acoustic Doppler current profilers (ADCPs) and a Neil-Brown conductivity-temperature probe. The ADCPs recorded at 1 Hz, and the Neil-Brown C-T probe recorded at 5 Hz. The ADCPs sampled the velocity field using 20 bins, with 0.5 m resolution and a 60-cm blanking distance from the vehicle. Velocity measurements from the ADCPs were mapped into a fixed interpolation grid (relative to Earth) for averaging, with 0.5 m vertical resolution and horizontal resolution that ranged from 40 m nearshore to 90 m offshore. Grid points sampled less than 15 times during a transect were omitted from further analysis.

2.3. Turbulent Microstructure

A Rockland Scientific Instruments Microrider 1000 was mounted in the nose of the vehicle to measure turbulent microstructure. The Microrider sensors, sampled at 512 Hz, included two airfoil shear probes that sampled transverse ($\partial v/\partial x$) and vertical ($\partial w/\partial x$) components (relative to vehicle reference frame) of shear, a FP07 thermistor, a SBE7-6000 microconductivity sensor, and two orthogonal accelerometers. The vehicle's speed through water, calculated using the mean of the first velocity bins of the two ADCPs, was used to convert raw counts recorded from probes to physical shear units, as well as in the conversion from frequency to

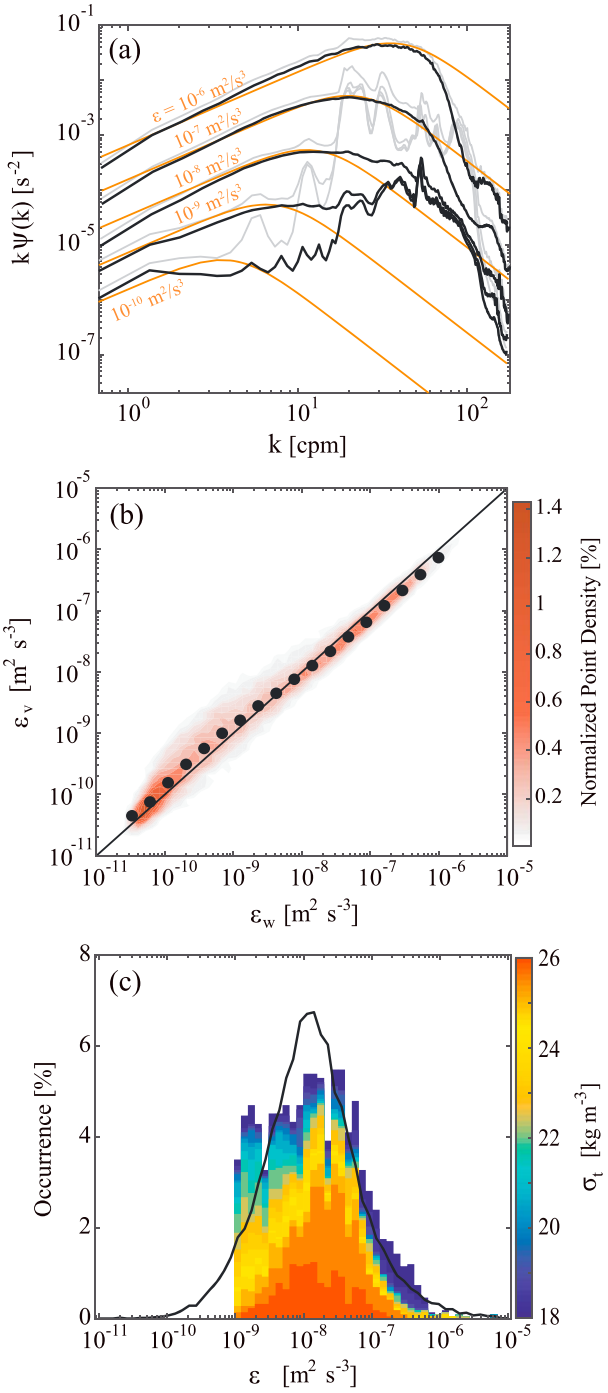

Figure 2. (a) Measured shear spectra averaged in decadal bins based on estimated dissipation rate (black lines), raw spectra prior to motion correction (gray lines), corresponding to the Nasmyth spectra for average dissipation rates (orange lines) in variance-preserving form. (b) Comparison of vertical and transverse dissipation estimates. Color scale indicates point density. (c) Comparison of Microrider dissipation rates and Thorpe-scaling estimates (black line) from a vertical microstructure profiler deployed near the autonomous underwater vehicle transect during T1. Color scale denotes density anomalies observed for binned autonomous underwater vehicle data.

wave number space. Assuming isotropy in the inertial subrange, the rate of TKE dissipation is related to shear as (Oakey, 1982):

$$\varepsilon = \frac{15}{2}\nu\overline{\left(\frac{\partial v}{\partial x}\right)^2} = \frac{15}{2}\nu\overline{\left(\frac{\partial w}{\partial x}\right)^2} = \frac{15}{2}\nu\int_0^\infty \Psi(k)dk, \quad (1)$$

where ν is the kinematic viscosity of seawater and the x-axis is along the vehicle's centerline. The estimation of dissipation rates from shear probes follows Macoun & Lueck (2004) and Lueck (2016) and is detailed in Text S1 in the supporting information.

3. Observations

3.1. Forcing Conditions

Energetic, downwelling-favorable winds were present in the 2 days preceding deployment, resulting in significant wave heights of 1.5 m and peak periods of 4 s (Figure 1). Winds became upwelling-favorable at the start of the mission (15 May 2015, 17:00 EST), clocking from easterly to southwesterly through the deployment. During the mission, wind speed averaged 7 m/s and the surface wave field was dominated by incoming Atlantic swell with significant wave heights of 0.8 m and typical peak periods of 8 s. The upwelling-favorable surface stress averaged 0.06 Pa during the event (Figure 1c). The timing of the cross-shore AUV transects is shown in relation to these conditions in Figure 1.

3.2. Shear Spectra and Dissipation Estimates

Figure 2a compares raw shear spectra measured via shear probes and cleaned spectra, which have had signals coherent with the Microrider's accelerometers removed following Goodman et al. (2006). Spectra have been bin-averaged based on estimated dissipation rates that correspond to fitted Nasmyth empirical spectra (Oakey, 1982). Nearly all vehicle motion was filtered out of the shear signals, with residual vehicle vibrations present at wave numbers greater than 20 cpm at low dissipation rates ($\varepsilon \leq 10^{-8}$ m^2/s^3). Measured shear spectra agreed well with the Nasmyth spectrum for wave numbers less than 50 cpm and showed a clear $k^{1/3}$ inertial subrange for dissipation rates down to 10^{-9} m^2/s^3. At low shear variances, vehicle vibrations overwhelmed environmental shear signals and prohibited estimation of dissipation rates below 10^{-9} m^2/s^3.

The ratio of dissipation estimates from transverse and vertical components of shear was used to evaluate errors in dissipation estimates that may stem from vehicle attitude and/or nonisotropic turbulence in the inertial subrange due to stable stratification. The mean ratio of dissipation estimates from the $\partial v/\partial x$ and $\partial w/\partial x$ components of shear (probes 1 and 2, respectively) was approximately 1 for both dives and climbs, indicating that there was no bias in shear estimates that would have resulted from directional flow distortion around the probes due to vehicle attitude (Figure 2b). However, there were significant reductions in $\partial w/\partial x$ relative to $\partial v/\partial x$ in regions of weak overturning and strong vertical stratification. This is consistent with a suppression of vertical velocities by buoyancy within the strongly stratified plume interior. As shown by Gargett et al. (1984) and Smyth and Moum (2000), the departure from isotropy at low-buoyancy Reynolds number can lead to an underprediction of the true dissipation rate when using only two terms in the strain rate tensor. At larger dissipation rates used in the estimation of the turbulent

buoyancy flux (Part 4), the vertical and transverse shear components were largely isotropic within the inertial subrange.

3.3. Plume Structure

A two-layer plume structure was observed, comprising an upper plume that was well-mixed (average density: 1,019 kg/m^3) and a lower plume with linearly varying vertical density stratification (average density: 1,022.3 kg/m^3; Figures 3a–3d). The bounds of the upper and lower layers of the plume were determined by finding local maxima in the Brunt-Vaisala frequency of $N^2 > 6.3 \times 10^{-3}$ s^{-2}. For reference, ambient shelf water in this region of the Mid-Atlantic Bight is 1,026 kg/m^3. Satellite sea surface temperature retrievals show that varying wind conditions over the course of multiple tidal cycles can lead to the generation of water masses with different fractions of estuarine water in the vicinity of the Chesapeake Bay mouth. The intermediate water represents the advection of older (lower) plume water, whereas the comparatively fresher near-surface core is newer.

To compare observations of plume mixing to existing theory, we consider a theoretical critical mixing depth derived from a simple model of Ekman physics and Richardson number stability (Fong & Geyer, 2001; Hetland, 2005; Lentz, 2004). Following Hetland (2005), the depth at which plume thickness satisfies stability theory can be estimated as

$$h_c = \frac{2\tau_y}{\rho_0 f}\sqrt{\frac{Ri_c}{h_f g \Delta\rho_f/\rho_0}}, . \tag{2}$$

The symbols are τ_y, alongshore wind stress; ρ_0, reference density of seawater; f, Coriolis parameter; $Ri = \Delta\rho g h/\rho_0 \Delta u^2$, bulk Richardson number; g, gravity; $\Delta\rho_f = \rho_f - \rho_0$, density difference between freshwater and ambient seawater; and h_f, freshwater thickness defined as

$$h_f = \int_{-H}^{\eta} \frac{\rho_0 - \rho}{\rho_0} \partial z, \tag{3}$$

where H represents full water column depth and η represents the free surface.

The mixing depth, calculated assuming a critical Richardson number of 2, was 2.5 m on average (green bars in Figure 3). As discussed in Hetland (2005), Ri_c is an effective value that should be higher than the theoretical value of 1 because the critical mixing depth model only includes Ekman-induced shear, whereas geostrophic and inertial flows also generate shear that contributes to plume mixing.

Within one inertial period of the onset of upwelling winds, the depth of the upper plume thinned as it was advected offshore, consistent with the Ekman response described in Fong and Geyer (2001). Note that while the thinning of the upper plume is consistent with the analytical critical depth, mixing within the lower plume occurred at depths greater than the critical depth, suggesting that Ekman straining was not a dominant mechanism driving scalar exchange within the lower plume. Furthermore, using a Ri_c value of 1 results in an underprediction of the mixing depth, suggesting that while Ekman shear played a role in mixing the upper plume, it was not the only process through which seawater was entrained into the plume.

The plume moved quickly offshore (T3, Figures 3c, 3g, and 3k), and the upper plume separated from the coast. Following the separation of the upper plume, an up-shelf alongshore current developed inshore of the upper plume with maximum velocities of 0.4 m/s near the surface and decreasing with depth consistent with Clark and Brink (1985); Austin and Lentz (2002), and Whitney and Garvine (2005). The upper plume continued to flow south following separation from the coast (T4, Figures 3d, 3h, and 3l).

A nonupwelling lateral circulation between 2 and 12 km offshore is evident following flood tides (T1 and T3). We speculate that this circulation was the result of flow over a ~6-m outcrop located 8 km north of the transect (at 36.5333°N, see red arrow in Figure 1a). Further details of the velocity structure within the plume will be reported elsewhere.

Figures 3m–3p show the gradient Richardson number, $Ri_g = N^2/S^2$, calculated using the Neil-Brown C-T probe (Figures 3a–3d) and gridded velocity observations (Figures 3e–3l). Throughout the mission, Ri_g frequently

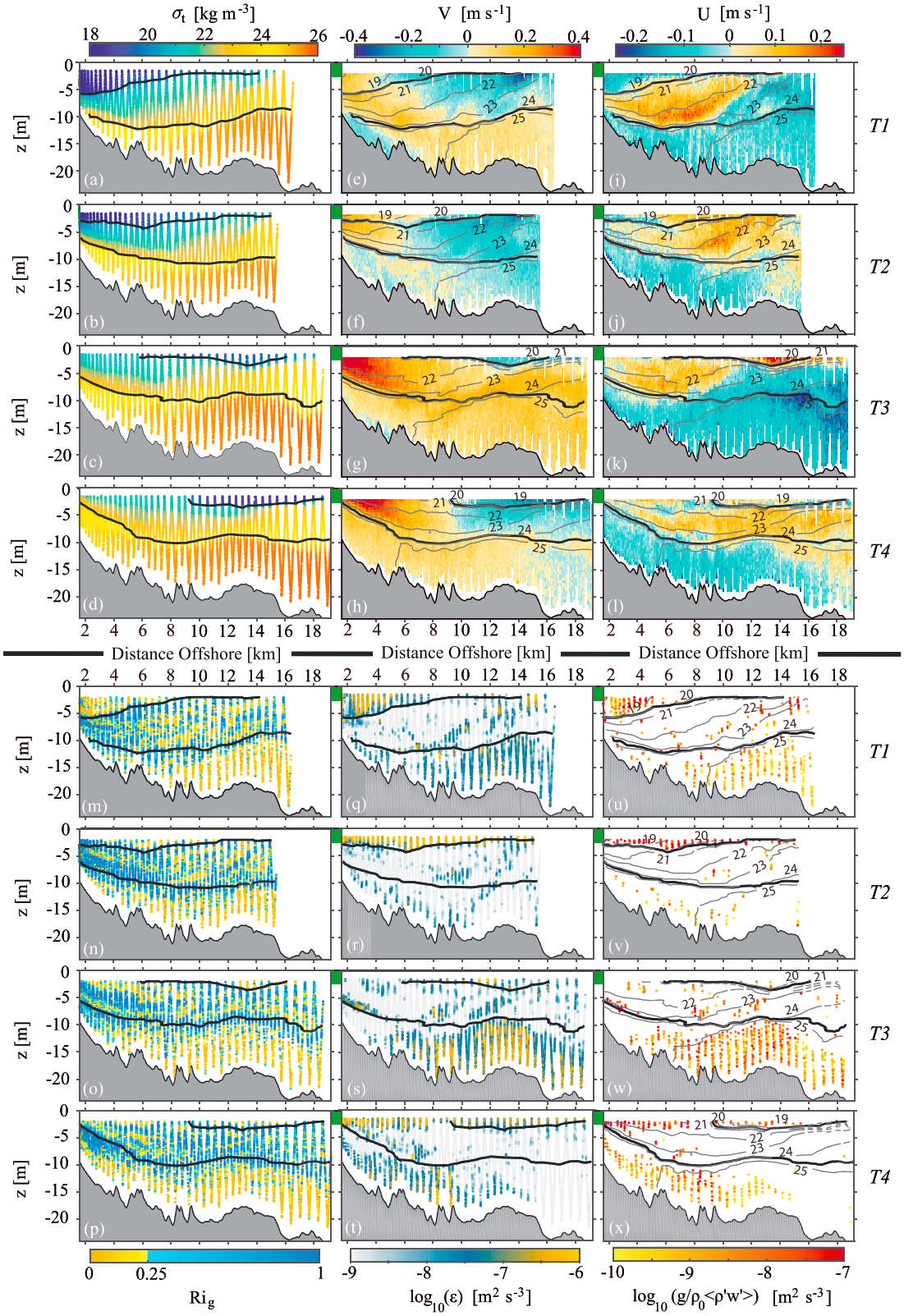

Figure 3. (a–d) Density anomaly. (e–h) Alongshore velocity (positive poleward). (i–l) Cross-shore velocity (positive offshore). (m–p) Gradient Richardson number values observed during each transect. Warm colors indicate $Ri_g < 0.25$. (q–t) Dissipation rates estimated from the shear probes. (u–x) Buoyancy flux estimated using equation (5). Gray lines are isopycnal contours. Black lines indicate base of upper and lower plume layers. Green vertical bars are the critical mixing depth (equation (2)).

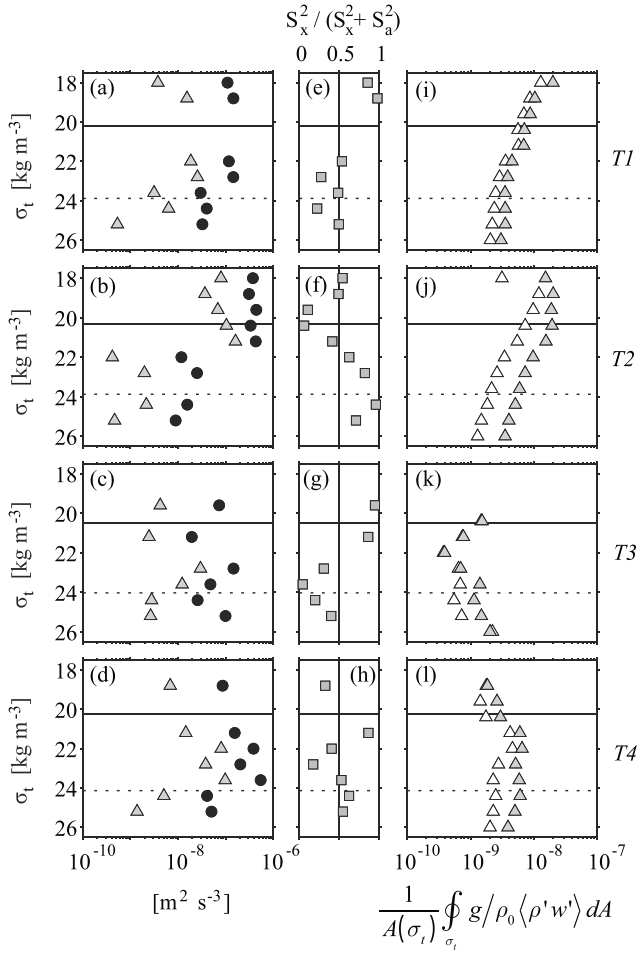

Figure 4. (a–d) Average dissipation rate (black circles) and buoyancy flux (white triangles) as a function of density class, σ_t for each transect. Solid/dotted lines denote average density at the base of the upper/lower plume. (e–h) Ratio of cross-shore to total vertical shear for each transect. (i–l) Plume-averaged buoyancy flux. Filled symbols show total buoyancy flux within the cross-sectional area A bounded by σ_t; open symbols indicate buoyancy flux estimated only using the vertically sheared cross-shore flow.

exceeded 0.25 at the base of the upper and lower layers, indicating that stable vertical stratification maintained the two-layer structure as the plume was advected offshore and limited the bottom boundary layer to <10 m above the seabed.

4. Vertical Turbulent Mixing and Salt Exchange

Microrider dissipation rates ranged from 10^{-6} m^2/s^3 to below the observable limit of 10^{-9} m^2/s^3 during the experiment (Figures 3q–3t) and agreed well with Thorpe-scaling estimates of dissipation from a microstructure profiler deployed on a wirewalker at 35.3671°N, 76.7764°W during T1 (Figure 2c). In areas of active overturning, the eddy diffusivity was O(10^{-5} m^2/s); this is lower than a diffusivity of O(10^{-4} m^2/s) inferred from the Hudson and Delaware Bay plumes from dye studies (Houghton et al., 2004, 2009), though winds were stronger (10 m/s) in those studies.

There was a nonlinear relationship between temperature and salinity during the experiment, such that plume waters ($s \leq 31$ psu) had a slope of $\Delta T/\Delta s = -0.41$ °C per psu, while ambient shelf waters had a slope of $\Delta T/\Delta s = -2.27$ °C per psu. Periodic noise in the FP07 thermistor prohibited direct estimation of the buoyancy flux from scalar dissipation rates, as both temperature and salinity contributed significantly to variations in density and conductivity. Instead, the buoyancy flux was estimated using the observed dissipation rate, density, and mean shear using an empirical parameterization of the flux Richardson number:

$$\langle \rho' w' \rangle = -K_z \frac{\partial \rho}{\partial z}, \tag{4}$$

where $K_z = \Gamma \varepsilon / N^2$ and $\Gamma = Ri_f/(1 - Ri_f)$. The flux Richardson number, $Ri_f = B/(B + \varepsilon)$, was modeled as a function of Ri_g and the buoyancy Reynolds number, $\varepsilon/\nu N^2$:

$$\left.\begin{array}{rl} Ri_f = 0.23 & Ri_g > 0.25 \\ Ri_f = 0.92 Ri_g & Ri_g \leq 0.25 \\ Ri_f = 0 & \varepsilon/\nu N^2 < 15 \end{array}\right\}, \tag{5}$$

This parameterization is based on observations of mixing efficiency in stratified estuaries (Holleman et al., 2016; Kay & Jay, 2003; MacDonald & Geyer, 2004) and the analytical model of Trowbridge (1992), which suggests that Ri_g is a plausible upper bound on Ri_f because reductions in mixing efficiency due to the attenuation of turbulent length scales near boundaries are captured by a corresponding reduction in Ri_g. When $\varepsilon/\nu N^2 < 15$, the combined effect of buoyancy and viscosity suppresses active overturning (Ivey & Imberger, 1991), which generally coincided with $Ri_g > 0.25$ during this experiment.

The buoyancy flux calculations highlight the transient and evolving nature of the plume in response to the upwelling wind. During the first 12 hr after the onset of upwelling winds (T1 and T2), shear-driven mixing within the lower plume occurred primarily beneath the offshore edge of the upper plume (e.g., 12–14 km offshore at depths of ~5–10 m, Figures 3m, 3n, 3q, and 3r). As the plume was advected offshore and adjusted to transient wind conditions, patchy mixing extended throughout the plume interior.

Figure 4 shows the average dissipation rate and turbulent buoyancy flux as a function of density class, σ_t, (Figures 4a–4d, binned in 0.8 kg/m^3 increments) and the estimated ratio of cross-shore shear to total shear (Figures 4e–4h). The variable contributions of along- and cross-shore shear in the upper plume appear related to changes in wind stress, as surface wind stress was higher during T2 and T4 than in T1 and T3 (Figure 1c), coincident with elevated dissipation rates in the upper ~3 m. Both tidal and wind forcing likely controlled

shear in the lower plume. In general, shear turbulence drove the largest buoyancy fluxes within the stratified interior of the plume; relative to the dissipation rate, buoyancy fluxes were lower near boundaries due to reduced mixing efficiency (equation (5)).

Prior to the onset of upwelling (T1), there was little to no buoyancy flux in density classes associated with the plume bases (Figures 3q, 3u, and Figure 4a). Cross-shore shear dominated total shear within the upper plume with alongshore and cross-shore shear production both contributing to the generation of buoyancy fluxes within the lower plume (Figure 4e). As upwelling progressed and the plume thinned and moved offshore (T2), direct wind mixing drove nearly all of the scalar exchange within the plume. The buoyancy flux was significant throughout all density classes associated with the upper plume, with the largest buoyancy fluxes due to entrainment at the base of the upper plume (Figure 4b); the effect of this mixing is evident in the loss of density classes in subsequent transects (though that the AUV did not sample the upper 1.5 m of the water column). While cross-shore shear dominated near the surface in T1, alongshore shear was primarily responsible for driving vertical mixing at the base of the upper and lower plumes in T2 (Figure 4f).

Following the separation of the upper plume from the coast (T3), surface mixing was minimal and the majority of scalar exchange resulted from mixing at higher density classes within the lower plume (Figure 4c). We speculate that these mixing hot spots (6–12 km offshore, Figures 3s and 3w) were a result of the interaction between offshore Ekman transport of the upper plume and topographically induced lateral circulation. We hypothesize that an internal stress divergence drove the mid-water column horizontal jet evident in Figure 3g, which elevated shear production and resulted in enhanced vertical mixing. Within this region, alongshore shear dominated the production of turbulence (Figure 4g) and drove the majority of mixing within the lower plume. Finally, stratification at the base of the lower plume limited the vertical extent of the up-shelf current shoreward of the upper plume, enhancing alongshore vertical shear at the base of the lower plume between 2 and 5 km offshore (Figures 3g, 3s, 4g, and 4h).

After approximately one inertial period (T4), shoaling of isopycnals due to upwelling exposed higher density classes to direct wind mixing (Figures 3d, 3t, and 3x) and alongshore shear eroded the base of the lower plume out to 4 km offshore. Cross-shore shear drove scalar exchange at the base of the upper plume (Figure 4h), while alongshore shear production generated mixing near the surface and at the base of the lower plume (Figure 4d). The highest average turbulent buoyancy fluxes occurred at density classes corresponding to the base of the lower plume.

In contrast to quasi-steady 2-D models of plume response to upwelling (Fong & Geyer, 2001; Lentz, 2004; Hetland, 2005), these results indicate that alongshore shear production can significantly contribute to mixing the far-field. To quantify the impact of neglecting the alongshore shear on estimating far-field mixing during upwelling, we estimate the buoyancy flux driven solely by a vertically sheared cross-shore flow. Assuming that Ri_f is a known function of Ri_g (equation (5)), based on measurements of total shear and stratification it can be shown (Text S2) that the cross-shore contribution to the total buoyancy flux is proportional to the ratio of cross-shore shear production to total shear production: $B_x \approx \left(S_x^2/S^2\right)B$.

Figures 4i–4l compare total turbulent buoyancy flux and estimated buoyancy flux driven solely by cross-shore shear production, within the area bounded by σ_t. Buoyancy flux decreases across density classes with gaps (Figures 4a–4d) because the bounding area increases in the absence of any mixing. Within the upper plume, cross-shore shear production generated 95% (T1), 40% (T2), 97% (T3), and 55% (T4) of the total buoyancy flux. Within the lower plume, the contribution of cross-shore shear production to the buoyancy flux was generally less. Consequently, neglecting vertical shear in the alongshore velocity could result in a significant underprediction of the plume-averaged buoyancy flux. This is most notable during T2, when mixing was strongest and neglecting alongshore shear production resulted in nearly a factor of 3 reduction in total entrainment. Both alongshore and cross-shore shear production contributed significantly to mixing within the plume suggesting that models based only on cross-shore Ekman straining are missing a significant fraction of total mixing within the far-field during the initial adjustment to upwelling.

5. Conclusions

Detailed observations of the response of the Chesapeake Bay far-field plume to an upwelling-favorable wind event were collected by REMUS 600 AUV. The observed plume comprised a fresher surface-trapped upper

plume overriding a saltier lower plume. Turbulent microstructure estimates of dissipation and buoyancy flux show that scalar exchange within the plume was complex during the transition to upwelling. Direct wind-driven mixing, while limited to the upper ~3 m of the water column by stable stratification within the lower plume, was a dominant driver of mixing during the transition to upwelling. Several studies have suggested that wind is the primary driver of mixing in the far-field of river plumes (Fong & Geyer, 2001; Hetland, 2005; Lentz, 2004). However, the phasing of tidal currents and adjustment of the plume to transient wind forcing (Fong & Geyer, 2001) may also play an important role in driving mixing within a plume, as we observed a significant contribution of along-shore shear to the buoyancy flux. Following separation of the upper plume from the coast, active mixing of the older, lower plume occurred along the shoreward edge. Thus, a combination of Ekman straining and vertically sheared alongshore flow contributed to heterogeneous and intermittent mixing within the plume.

These novel observations illustrate the complexity of scalar mixing within the far-field of a river plume during the transition to upwelling. Such intermittency and spatial variability underscore the importance of resolving transient features in measurements and the need for numerical models to incorporate realistic bathymetry at high resolution in order to determine the fate of terrestrially derived materials exported along continental shelves.

Acknowledgments
The authors are indebted to Dave Loewensteiner for field assistance and AUV preparation. We also thank Ken Roma, captain of the *R/V Arabella*, for assistance in deployment and recovery of the AUV, and two anonymous reviewers, whose constructive comments improved the manuscript. Data are available in ASCII format in the supporting information. This work was supported by NSF awards OCE-1334398, OCE-1745258, and OCE-1334231.

References

Austin, J. A., & Lentz, S. J. (2002). The inner shelf response to wind-driven upwelling and downwelling. *Journal of Physical Oceanography*, *32*, 2171–2193.

Castelao, R., Scholfield, O., Glenn, S., Chant, R., & Kohut, J. (2008). Cross-shelf transport of freshwater on the New Jersey shelf. *Journal of Geophysical Research*, *113*, C07017. https://doi.org/10.1029/2007JC004241

Chant, R. J., Wilkin, J., Zhang, W., Choi, B., Hunter, E., Castelao, R., et al. (2008). Dispersal of the Hudson River plume in the New York Bight: Synthesis of observational and numerical studies during LaTTE. *Oceanography*, *21*(4), 148–161. https://doi.org/10.5670/oceanog.2008.11

Chen, F., & MacDonald, D. G. (2006). Role of mixing in the structure and evolution of a buoyant discharge plume. *Journal of Geophysical Research*, *111*, C11002. https://doi.org/10.1029/2006JC003563

Clark, A. J., & Brink, K. H. (1985). The response of stratified, frictional flow of shelf and slope waters to fluctuating large-scale, low-frequency wind forcing. *Journal of Physical Oceanography*, *15*(4), 439–453. https://doi.org/10.1175/1520-0485(1985)015<0439:TROSFF>2.0.CO;2

Fer, I., Peterson, A. K., & Ullgren, J. E. (2014). Microstructure measurements form an underwater glider in the turbulent Faroe Bank Channel overflow. *Journal of Atmospheric and Oceanic Technology*, *31*(5), 1128–1150. https://doi.org/10.1175/JTECH-D-13-00221.1

Fong, D. A., & Geyer, W. R. (2001). Response of a river plume during an upwelling favorable wind event. *Journal of Geophysical Research*, *106*(C1), 1067–1084. https://doi.org/10.1029/2000JC900134

Fong, D. A., Geyer, W. R., & Signell, R. P. (1997). The wind-forced response on a buoyant coastal current: Observations of the western Gulf of Maine plume. *Journal of Marine Systems*, *12*(1-4), 69–81. https://doi.org/10.1016/S0924-7963(96)00089-9

Gargett, A. E., Osborn, T. R., & Nasmyth, P. W. (1984). Local isotropy and the decay of turbulence in a stratified fluid. *Journal of Fluid Mechanics*, *144*(1), 231–280. https://doi.org/10.1017/S0022112084001592

Garvine, R. W. (1987). Estuary plumes and fronts in shelf waters: A layer model. *Journal of Physical Oceanography*, *17*(11), 1877–1896. https://doi.org/10.1175/1520-0485(1987)017<1877:EPAFIS>2.0.CO;2

Goodman, L., Levine, E. R., & Lueck, R. G. (2006). On measuring the terms of the turbulent kinetic energy budget from an AUV. *Journal of Atmospheric and Oceanic Technology*, *23*(7), 977–990. https://doi.org/10.1175/JTECH1889.1

Gregg, M. C. (1987). Diapyncal mixing in the thermocline: A review. *Journal of Geophysical Research*, *92*(C5), 5249–5284. https://doi.org/10.1029/JC092iC05p05249

Hetland, R. D. (2005). Relating river plume structure to vertical mixing. *Journal of Physical Oceanography*, *35*(9), 1667–1688. https://doi.org/10.1175/JPO2774.1

Hetland, R. D. (2010). The effects of mixing and spreading on density in near-field river plumes. *Dynamics of Atmospheres and Oceans*, *49*(1), 37–53. https://doi.org/10.1016/j.dynatmoce.2008.11.003

Holleman, R. C., Geyer, W. R., & Ralston, D. K. (2016). Stratified turbulence and mixing in a salt wedge estuary. *Journal of Physical Oceanography*, *46*(6), 1769–1783. https://doi.org/10.1175/JPO-D-15-0193.1

Horner-Devine, A. R. (2009). The bulge circulation in the Columbia River plume. *Continental Shelf Research*, *29*(1), 234–251. https://doi.org/10.1016/j.csr.2007.12.012

Horner-Devine, A. R., Hetland, R. D., & MacDonald, D. G. (2015). Mixing and transport in coastal river plumes. *Annual Review of Fluid Mechanics*, *47*(1), 569–594. https://doi.org/10.1146/annurev-fluid-010313-141408

Houghton, R. W., Chant, R. J., Rice, A., & Tilburg, C. (2009). Salt flux into coastal river plumes: Dye studies in the Delaware and Hudson River outflows. *Journal of Marine Research*, *67*(6), 731–756. https://doi.org/10.1357/002224009792006142

Houghton, R. W., Tilburg, C. E., Garvine, R. W., & Fong, A. (2004). Delaware River plume response to a strong upwelling-favorable wind event. *Geophysical Research Letters*, *31*, L07302. https://doi.org/10.1029/2003GL018988

Ivey, G. N., & Imberger, J. (1991). On the nature of turbulence in a stratified fluid. I: The energetics of mixing. *Journal of Physical Oceanography*, *21*(5), 650–658. https://doi.org/10.1175/1520-0485(1991)021<0650:OTNOTI>2.0.CO;2

Kay, D. J., & Jay, D. A. (2003). Interfacial mixing in a highly stratified estuary. 1. Characteristics of mixing. *Journal of Geophysical Research*, *108*(C3), 3072. https://doi.org/10.1029/2000JC000252

Kilcher, L., & Nash, J. D. (2010). Structure and dynamics of the Columbia River tidal plume front. *Journal of Geophysical Research*, *115*, C05S90. https://doi.org/10.1029/2009JC006066

Kilcher, L., Nash, J. D., & Moum, J. N. (2012). The role of turbulence stress divergence in decelerating a river plume. *Journal of Geophysical Research*, *117*, C05032. https://doi.org/10.1029/2011JC007398

Lentz, S. J. (2004). The response of buoyant coastal plumes to upwelling-favorable winds. *Journal of Physical Oceanography*, *34*(11), 2458–2469. https://doi.org/10.1175/JPO2647.1

Lentz, S. J., & Largier, J. (2006). The influence of wind forcing on the Chesapeake Bay buoyant coastal current. *Journal of Physical Oceanography*, *36*(7), 1305–1316. https://doi.org/10.1175/JPO2909.1

Lueck, R. (2016). Calculating the rate of dissipation of turbulent kinetic energy, *Rockland Scientific International*, RSI Technical Note 028.

MacDonald, D. G., & Geyer, W. R. (2004). Turbulent energy production and entrainment at a highly stratified estuarine front. *Journal of Geophysical Research*, *109*, C05004. https://doi.org/10.1029/2003JC002094

MacDonald, D. G., Goodman, L., & Hetland, R. D. (2007). Turbulent dissipation in a near-field river plume: A comparison of control volume and microstructure observations with a numerical model. *Journal of Geophysical Research*, *112*, C07026. https://doi.org/10.1029/2006JC004075

Macoun, P., & Lueck, R. (2004). Modeling the spatial response of the airfoil shear probe using different sized probes. *Journal of Atmospheric and Oceanic Technology*, *21*(2), 284–297. https://doi.org/10.1175/1520-0426(2004)021<0284:MTSROT>2.0.CO;2

Mazzini, P. L. F., Barth, J. A., Shearman, R. K., & Erofeev, A. (2014). Buoyancy-driven coastal currents off Oregon during fall and winter. *Journal of Physical Oceanography*, *44*(11), 2854–2876. https://doi.org/10.1175/JPO-D-14-0012.1

Mazzini, P. L. F., & Chant, R. J. (2016). Two-dimensional circulation and mixing in the far field of a surface-advected river plume. *Journal of Geophysical Research: Oceans*, *121*, 3757–3776. https://doi.org/10.1002/2015JC011059

McCabe, R. M., MacCready, P., & Hickey, B. M. (2009). Ebb tide dynamics and spreading of a large river plume. *Journal of Physical Oceanography*, *39*(11), 2839–2856. https://doi.org/10.1175/2009JPO4061.1

Nash, J. D., Kilcher, L. F., & Moum, J. N. (2009). Structure and composition of a strongly stratified, tidally pulsed river plume. *Journal of Geophysical Research*, *114*, C00B12. https://doi.org/10.1029/2008JC005036

Oakey, N. S. (1982). Determination of the rate of dissipation of turbulent kinetic energy from simultaneous temperature and velocity shear microstructure measurements. *Journal of Physical Oceanography*, *12*(3), 256–271. https://doi.org/10.1175/1520-0485(1982)012<0256:DOTROD>2.0.CO;2

Smyth, W. D., & Moum, J. N. (2000). Anisotropy of turbulence in stably stratified mixing layers. *Physics of Fluids*, *12*(6), 1343–1362. https://doi.org/10.1063/1.870386

Trowbridge, J. H. (1992). A simple description of the deepening and structure of a stably stratified flow driven by a surface stress. *Journal of Geophysical Research*, *97*(C10), 15,529–15,543. https://doi.org/10.1029/92JC01512

Valle-Levinson, A., Wong, K.-C., & Bosley, K. T. (2001). Observations of the wind-induced exchange at the entrance of Chesapeake Bay. *Journal of Marine Research*, *59*(3), 391–416. https://doi.org/10.1357/002224001762842253

Whitney, M. M., & Garvine, R. W. (2005). Wind influence on a coastal buoyant outflow. *Journal of Geophysical Research*, *110*, C03014. https://doi.org/10.1029/2003JC002261

Yankovsky, A. E., & Chapman, D. C. (1997). A simple theory for the fate of buoyant coastal discharges. *Journal of Physical Oceanography*, *27*(7), 1386–1401. https://doi.org/10.1175/1520-0485(1997)027<1386:ASTFTF>2.0.CO;2